

Article

Case Study of Single-Controllable Microgrid: A Practical Implementation

Geovane L. Reis ^{1,2,*}, Danilo I. Brandao ^{1,*}, João H. Oliveira ¹, Lucas S. Araujo ¹ and Braz J. Cardoso Filho ¹

¹ Graduate Program in Electrical Engineering, Federal University of Minas Gerais (UFMG), Belo Horizonte 31270-901, Brazil

² Institute of Technological Sciences (ICT), Campus of Itabira, Federal University of Itajubá (UNIFEI), Itabira 35903-087, Brazil

* Correspondence: geovanereis@unifei.edu.br (G.L.R.); dibrandao@ufmg.br (D.I.B.)

Abstract: This paper presents the implementation of a single-controllable microgrid in the engineering school of the Federal University of Minas Gerais using commercial devices. Such a microgrid exchanges controllable active and reactive power terms with the upstream grid, proportionally shares active/reactive power among the battery-based DERs and endows the microgrid with the capability of operating in both grid-connected and islanded modes. The energy storage system is composed of three different battery technologies: lead-acid, lithium-ion and sodium–nickel, which are coordinately controlled according to their inherent features. A usable average energy control is proposed to avoid mismatches between the batteries' states of charge. The single-controllable microgrid performs the following services: self-consumption, energy time shift, peak-shaving and reactive power support to the upstream grid. The coordinated secondary control and the operating modes of the microgrid were validated by means of full-scale experimental results using commercial devices. The lithium-ion battery showed the best performance in terms of round-trip efficiency, 93% over 85% (lead-acid) and 81% (sodium–nickel). The results demonstrated the microgrid's capability of delivering ancillary services at the connection with the upstream grid, and proportionally exploiting the dispersed battery banks. In addition, the challenges of practical implementation were analyzed.

Keywords: battery; distributed generation; hosting capacity; microgrid; power dispatch



Citation: Reis, G.L.; Brandao, D.I.; Oliveira, J.H.; Araujo, L.S.; Cardoso Filho, B.J. Case Study of Single-Controllable Microgrid: A Practical Implementation. *Energies* **2022**, *15*, 6400. <https://doi.org/10.3390/en15176400>

Academic Editor: Alon Kuperman

Received: 14 July 2022

Accepted: 22 August 2022

Published: 1 September 2022

Publisher's Note: MDPI stays neutral with regard to jurisdictional claims in published maps and institutional affiliations.



Copyright: © 2022 by the authors. Licensee MDPI, Basel, Switzerland. This article is an open access article distributed under the terms and conditions of the Creative Commons Attribution (CC BY) license (<https://creativecommons.org/licenses/by/4.0/>).

1. Introduction

Currently, microgrids (MGs) are appealing solutions to the large proliferation of power converters that are embedded in distributed energy resources (DERs) and electric vehicles (EVs) that must exchange power with the distribution power system [1]. The poor coordination of such elements results in an overall hosting capacity (hosting capacity is it the capacity of sources and loads that a certain grid or microgrid can host) (HC) limit [2] of about 20–50% of MV/LV transformer rated power, according to the pre-existing grid infrastructure [3]. The bottlenecks usually are the following: overvoltage, conductor thermal capacity and voltage imbalance [4].

There are three approaches to raise the HC limit: (i) grid reinforcement, (ii) autonomous ancillary services in DERs, and (iii) coordination of loads and DERs in MGs. The first approach requires prompt and significant augmentation of the grid, and has consequently been avoided thus far. The second approach is currently being applied, as recommended by the IEEE Std. 1547–2018 [5]; the third approach is based on single-controllable MG models [6]. This latter approach involves the hierarchical interconnection of smaller MGs (i.e., picogrids, nanogrids, microgrids, etc.) to larger MGs (i.e., milligrids, megagrids, gigagrids, etc.) [7].

Although the definitions of such variations of MG are not consolidated in literature, herein an advanced MG structure must be able to do the following:

- perform power sharing among the DERs in order to minimize the line power losses;
- regulate the active and reactive power exchanged with the upstream grid as a single-controllable entity;
- have the capability of operating in both grid-connected and islanded modes in order to ensure high levels of electrical reliability.

If one of the aforementioned features is not present in the power structure, then it should not be classified as single-controllable MG. The features of a single-controllable entity are also referred to in [5] when stating that the standard applies to interconnection of multiple DERs, considering the sum of their aggregate nameplate ratings.

A. Literature Review

The growing demand for microgrids that allow 100% renewable energy in current electrical systems (i.e., maximum HC), with reliability and stability, has contributed to a significant increase in MG laboratories and/or test beds. These laboratories have become a fundamental tool for researchers and university students. In addition, they can be used to validate and develop devices as well as adequate control strategies for each type of MG. Due to the rapid evolution of devices that make up MGs, as well as the costs and time to implement a physical laboratory, many universities and research centers have opted for the development of virtual laboratories. These labs feature reduced costs and offer a greater degree of freedom and flexibility for research activities [8]. The authors in [9] presented a virtual laboratory that allows the study of the blocks that compose an MG. The lab was developed using NI LabVIEW, MATLAB/Simulink software and Microsoft.Net Core open-source platform. A virtual laboratory based on the student version of MATLAB/Simulink was proposed in [10]. The project aims to prepare students for the job market, through closer contact with the building blocks of MGs. However, the great flexibility of simulations comes with a low fidelity of the results. As a workaround, using test beds based on hardware-in-the-loop (HIL) simulations are employed. HIL setups allow users to obtain simulation results that are similar to those obtained with real test beds, in addition to providing good flexibility [11].

In [12], a universal test bed for an MG based on hardware-in-the-loop (HIL) was proposed. The experimental test platform is composed of a real-time digital simulator (RTDS) that is responsible for simulating the MG, a communication interface, an energy management system (EMS) and a bi-directional converter (back-to-back) responsible for connecting the MG with the laboratory's local utility grid. The power-hardware-in-the-loop (PHIL) technique was used in [13] for the development of a teaching laboratory focused on the study of MGs as well as the devices that compose them. This configuration allows the connection of a physical component (e.g., a photovoltaic inverter) to a simulated network in real time, as used in [12]. The study focused on the grid-connected operation of an MG and the exchange of energy between the devices that compose it. The authors in [14] used the PHIL simulation technique to validate the operation of an islanded MG controller. However, communication between the central controller and the devices, as well as the energy exchange between the microgrid devices, were not evaluated.

Implementations that use the HIL technique and its variations are a dynamic tool for the study and development of smart grids. However, this kind of setup still has a high acquisition cost, which often inhibits its use by a larger number of researchers and students [15]. On the other hand, test beds with real devices guarantee high fidelity to the real application, although they are not very flexible as a result of the intrinsic characteristics of each device and developed project. In [16], the authors proposed a modular test bed for microgrid studies to use in a laboratory setting. However, the experimental framework is still under development, and only incipient experimental results of the communication between the key elements of MG were presented. In [17], the authors showed how to design a smart grid test bed for educational purposes using open-source software, which allows for the analysis and application of the most diverse resources applied in smart grids. The idea of applying an open-source framework is to allow for greater interaction

between students and researchers from different universities, and consequently continuous improvement of the framework. The development of the experimental part is still in the testing phase and will be presented in future papers.

A control structure for power sharing using the droop technique between neighboring MGs was proposed in [18]. The test bed is based on two single-phase converters and two photovoltaic simulators; the control structure was developed in NI LabVIEW software and embedded in the sbRIO-9683 development board. In [19], the development of a central controller for the MG laboratory at the University of Aalborg, Denmark was presented. The complete control system applied in this laboratory is based on the hierarchical strategy for MGs, and includes primary, secondary and tertiary controls. The primary control loops were developed in MATLAB/Simulink and compiled in dSPACEs. The central controller responsible for supervision and control was developed in LabVIEW. Renewable energy sources were emulated by a DC source. Experimental results on compensation of voltage and frequency deviation and voltage imbalance in an islanded MG were presented. In [20], the authors presented the design and implementation of a microgrid laboratory for teaching. The structure is composed of a wind turbine, photovoltaic energy, three DC/DC converters (batteries, PV and wind) and a DC/AC converter responsible for connecting the energy sources to the utility grid. Simulated and experimental results were presented. In [21], the authors presented the structure of The Canadian Renewable Energy Laboratory (CANREL). The article presents the MG structure that was built in a container approach and integrates rooftop photovoltaic generation, photovoltaic and wind generation simulator, a lithium-battery equipped battery management system (BMS), diesel generator, loads and a hierarchical central control unit. The structure allows for operation in different modes; however, the research is focused more on islanded operation of the system. An energy management system for an MG applied to smart buildings was proposed in [22]. In order to validate the strategy, the authors used the MG laboratory at the University of Sapienza in Rome, which is composed of commercial devices such as a lithium BESS, solar PV and a diesel generator. The strategy focuses on connected operation and the reduction in energy costs via management of MGs.

As presented in IEEE Std. 2030.8–2018 [23], there is a tradeoff between the flexibility of test beds using microgrid controllers and the fidelity of their results. In other words, although simulations allow a wide range of applications and tests, they cannot portray practical problems with high fidelity, and must be used principally in the preliminary stages of development. Test benches with real devices can achieve high fidelity in the results, but have low flexibility. Finally, simulations using HIL techniques and their variations represent an approach that falls somewhere in the middle.

The in-practice evaluation for single-controllable MGs is valuable to validate typical issues that are encountered only in practical implementation, such as the non-idealities of communication links as random latencies in shared data networks due to traffic data. The overall latency comprises the communication latency in addition to the inherent time required for inverters to update their output power after receiving a power command. In current commercial devices, this requires tens of seconds, and latencies are directly related to the MG time response.

In summation, Table 1 compares single-controllable MGs using different approaches in coordinated MG control to perform ancillary services. Note that none of them, except for this manuscript, have validated the operation of single-controllable MGs through experimental configuration using commercial devices with active function (i.e., P and Q control), and coordinated to perform ancillary services with the upstream grid.

Regarding energy storage systems, MGs equipped with several batteries of different technologies and/or ages are challenged in exploiting the maximum usable energy of every unit. The usable energy is defined as the area between minimum and maximum SoC values, and may also be a function of the released capacity [24], as typically for lithium-ion it is 15–95%, lead-acid 70–90% and sodium–nickel 35–95%. These numbers represent 80%, 20% and 60% of the depth of discharge to the nameplate capacity for lithium-ion, lead-acid and

sodium–nickel technologies, respectively. If no coordinated control of usable energy is applied to the MG structure, then it will not be able to fully exploit the stored energy in all dispersed battery banks, since the proportional exploitation will limit to the first bank that reaches its maximum or minimum SoC value. It is noteworthy that none of the test benches presented in Table 1 used different battery technologies in their structures.

Table 1. Comparison between state-of-the-art single-controllable microgrids.

| Ref.-Year | Single-Controllable MG Control Approach | MG Ancillary Service | Results/Validation |
|-----------|---|---|-------------------------------|
| [12]-2014 | Yes—centralized | demand–response, island | PHIL |
| [13]-2017 | Yes—centralized, droop control | peak-shaving, regulation of voltage | PHIL |
| [19]-2015 | Yes—centralized, droop control | regulation of freq. and voltage, island | exp. setup with lab devices |
| [20]-2021 | Yes—centralized | demand–response | exp. setup with lab devices |
| [21]-2020 | Yes—centralized | demand–response, island | exp. setup with lab devices |
| [22]-2021 | Yes—centralized | self-consumption | exp. setup with lab devices |
| [25]-2014 | yes—master-slave cooperative control | power factor control, island | exp. setup with lab devices |
| [26]-2018 | yes—distributed leader follower control | power flow control, island | time-domain simulations |
| [27]-2019 | yes—model-based E-LAN approach | power steering in feeders, island | MatLab simulation |
| [28]-2019 | yes—droop control | intra-phase power control, isolated | PSCAD simulation |
| [29]-2020 | yes—distributed two level control | regulation of freq. and voltage, island | exp. setup with lab devices |
| [30]-2020 | yes—model-based E-LAN approach | power flow control, island, demand–response | real-time validation |
| [31]-2020 | yes—centralized logic and predictive control | spinning power reserve | intra-day simulations |
| [32]-2021 | yes—model-free power-based control | volt-var function, spinning reserve | MatLab simulation |
| Herein | yes—model-free power-based control with average energy weight | self-consumption, energy time shift, reactive power support, island | exp. setup with comm. devices |

B. Paper Contributions and Organization

This paper depicts a practical implementation of a single-controllable MG developed in the School of Engineering at Federal University of Minas Gerais (UFMG), Brazil, supported by Petrobras S.A. Such an MG is deployed (i) using off-the-shelf commercial equipment that complies with current grid codes; (ii) is oriented to regulate active/reactive power at the PCC with the mains; and (iii) is based on a generic model-free formulation that considers arbitrary connection of inverters. The battery-based DERs use lead-acid, lithium-ion and sodium–nickel technologies. In order to avoid mismatches between the states of charge of different battery technologies, this paper proposes (iv) a usable average energy control embedded in the secondary MG control. Then, considering the above-mentioned scenario and incorporated features (i.e., from (i) to (iv)), the contributions of this paper are as follows:

- The development of a model-free and centralized coordinated control strategy, which steers different battery-based DERs to achieve proportional sharing among DERs and equalizes the usable energy of batteries;
- A coordination strategy that also supports the rarely addressed concept of single-controllable MG with arbitrarily connected (line-to-line inverters in three-phase four-wire grid) inverters that perform self-consumption and reactive power support, thereby lessening the burden of power dispatch of the upstream grid, if desired;
- Experimental results of an in-practice MG implementation using commercial inverters that apply controllable ancillary services at the MG point of connection to the upstream grid, coordinating battery banks of different technologies;

- Development of a test bench for microgrids with commercial inverters and the use of open-source software, which facilitates its reproduction by other universities that seek to develop teaching and research laboratories focused on microgrids.

This paper is organized as follows: Section 2 describes the MG structure and control organization. Section 3 presents the coordinated control used to steer DERs, the proposed usable average energy control and the power and communication elements. Section 4 shows the experimental results that consider self-consumption, energy time shift, grid support and island mode. Finally, Section 5 concludes this paper.

2. Microgrid Structure and Control

A. Microgrid structure

Figure 1 shows the centralized three-phase four-wire MG structure that has been running since July/2021. It consists of a centralized backup grid-forming system (full four-quadrant grid simulator TC.ACS); CB₁ and CB₂ breakers responsible for switching the MG operating modes, i.e., grid connected (CB₁ closed and CB₂ open) and islanded (CB₁ open and CB₂ closed); CB₃ and CB₄ breakers to disconnect non-critical loads under island mode; a PV power system with a 12-kilowatt three-phase inverter from PHB-PHB12KN-DT; a programmable power load (regenerative four-quadrant AC load NHR 9430); an AC bus for critical load connection (i.e., island operation transitioning); and three battery inverters of 6 kW each from SMA (sunny island 6.0 H), supplied by three different battery banks of about 5 kW/15 kWh of usable energy: lead-acid (48 V–1320 Ah)—six strings in parallel composed of four batteries in each of 12MS234 from Moura; lithium-ion (48 V–500 Ah)—five modules in parallel of UPLFP48 from Unipower; and sodium–nickel (48 V–400 Ah)—two modules in parallel of 48TL200 from FZSONICK. It is worth highlighting that the battery inverters are in delta connection due to their required voltage level (about 230 V). Such an MG is coordinated by means of a centralized controller, a Raspberry Pi B3+ embedded in a power node device in star connection at the MG PCC. The power node measures grid voltages and currents and computes the active and reactive powers, transferring them to the central controller (CC) through a ModBus RTU (RS-485) communication link. It also performs non-critical load shedding (CB₃ and CB₄) during MG-islanded operation. The CC interoperability with the battery inverters is based on ModBus TCP. Finally, Figure 2 shows a picture of the actual installation at UFMG.

B. Microgrid protection system

By using commercial off-the-shelf devices in compliance with current grid codes, the proposed MG already inherits several protections defined in the standards and embedded in these devices. SMA Sunny Island 6.0H inverters, for example, have the following protections: AC short-circuit/AC overload; DC reverse polarity protection/DC fuse; overtemperature/battery deep discharge; and overvoltage category as per IEC 60664. The PHB inverter model PHB12KN-DT used in the photovoltaic plant has the following protections: DC reverse polarity protection; DC/AC surge protection; insulation resistance monitoring; AC short-circuit protection; ground fault monitoring; anti-islanding protection. In addition, lithium-ion and sodium–nickel batteries are equipped with a battery management system (BMS) that provides specific battery protection. In addition to the native protections of commercial devices, three switchboards are included in the MG, as shown in Figure 2. The DC switchboard is responsible for protecting the batteries; the SMAs switchboard is responsible for protecting the AC side of the SMAs; and finally, the central switchboard is responsible for protecting loads in general, and for connecting the MG to the utility grid. The switchboards, in addition to contributing to the protection of the MG, allow the circuit to be disconnected during maintenance processes.

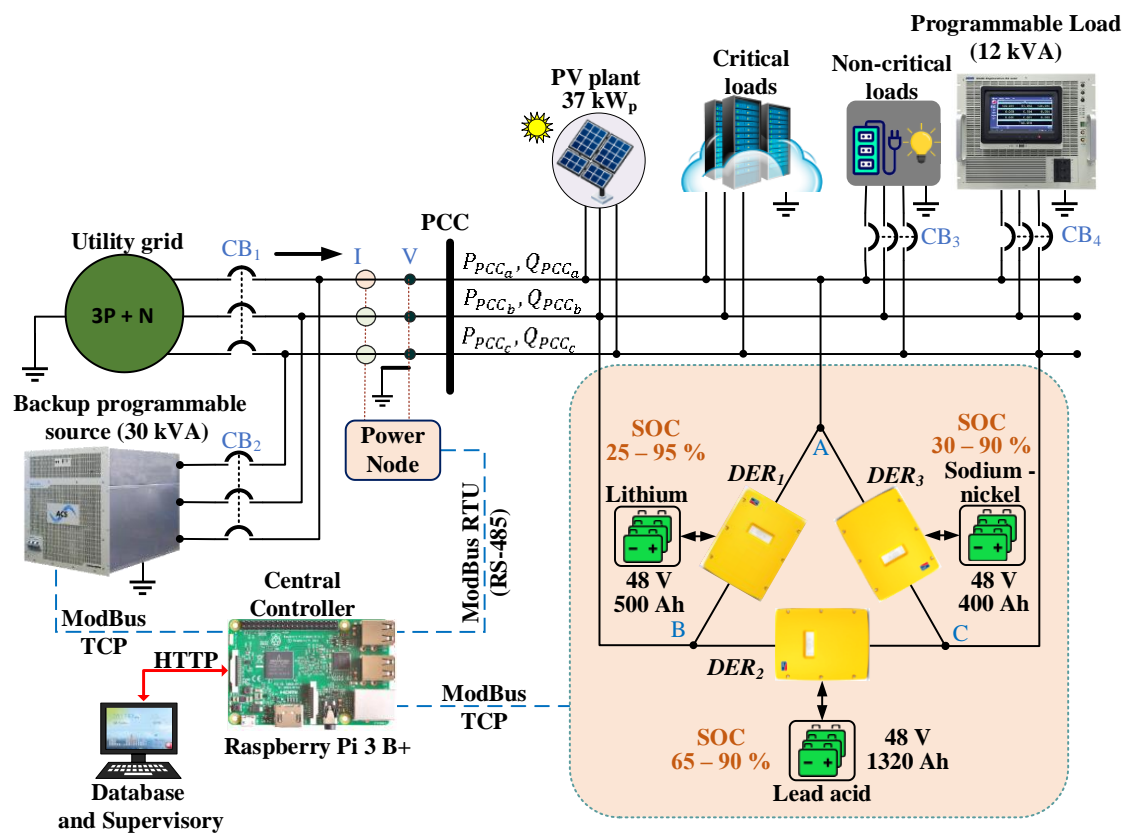


Figure 1. Block diagram of the single-controllable microgrid.

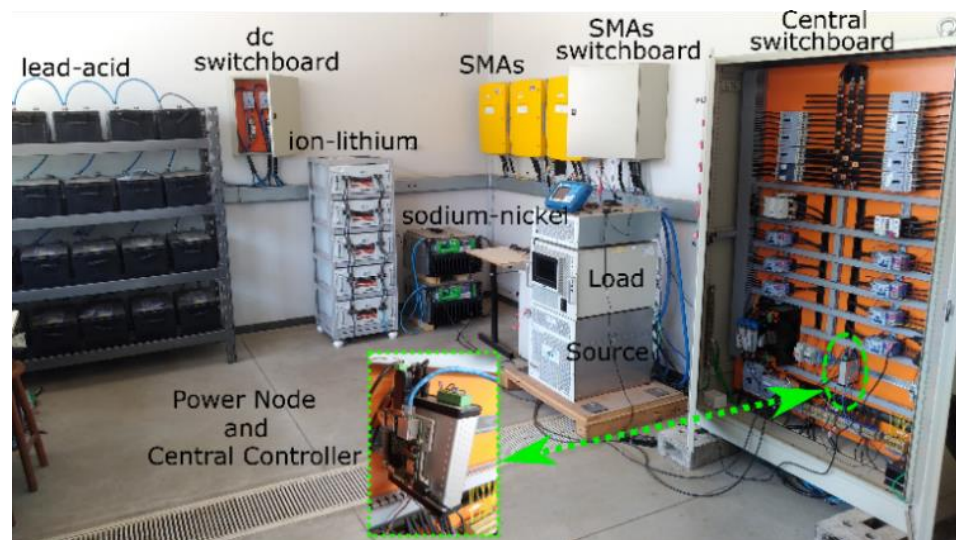


Figure 2. Actual installation of the single-controllable microgrid at UFMG, Brazil.

C. Control and Organization

The hierarchical MG architecture is adopted to coordinate the local operation of DERs, and to provide specific ancillary services to the single-controllable MG, as shown in Figure 3. The hierarchical control uses a communication link to exchange data between the CC and the distributed DERs. The content of the data transmitted from DERs to the CC comprises the current status of output power as well as rated and generation capacities. The reverse path of communication is the scaling coefficients used to set the power references in the local controller of DERs.

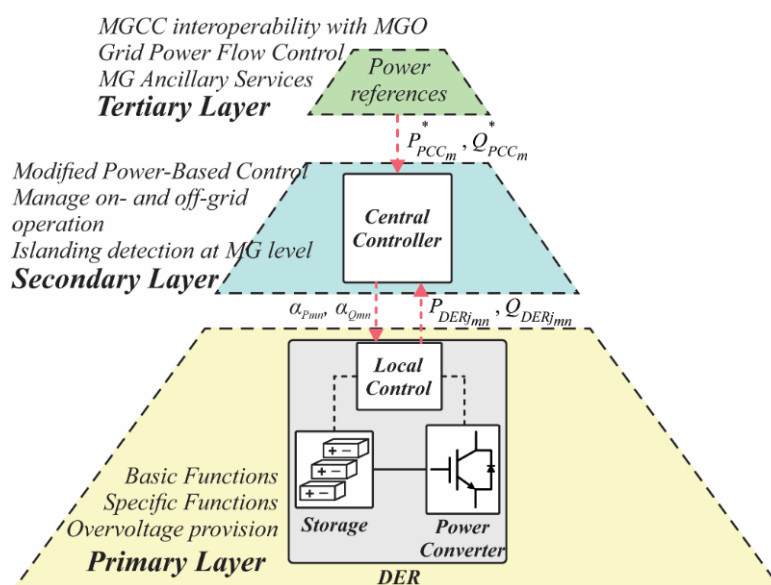


Figure 3. Microgrid hierarchical control organization.

The hierarchical architecture is based on the well-known concept of layers [33]. The primary layer is responsible for the local operation of each DER. It offers basic services (e.g., current/voltage control, grid synchronization) and specific functions (e.g., anti-islanding, voltage provision, etc.). The primary layer is devised by the manufacturers of the DERs; the basic functions do not rely on communication, while the specific functions can be steered using communication [34,35]. The photovoltaic plant is also composed of commercial inverters. Details such as the topology used, the structure of the output filter, control loops and the strategy used in the maximum power point tracking (MPPT) method are not provided by the manufacturer. The photovoltaic plant has a passive function in the microgrid; that is, it is not a dispatchable energy source.

The secondary layer consists of the modified power-based control (MPBC) algorithm [36], which defines the scaling coefficients and therefore, the active and reactive power references of the DERs. The secondary layer can achieve several targets (e.g., proportional power sharing among DERs, grid power flow control, voltage regulation and imbalance compensation) [37].

Finally, the tertiary layer performs the interoperability between the MG CC and the MG operator (MGO). Such interoperability sets the middle- and long-term power-flow as well as ancillary services scheduling at the MG level. It usually takes into consideration the MG's own limits and interests, the upstream grid requirements and the interoperability between the MGO with the distribution system operator (DSO).

In [38], an example of coordinated control applied to a distributed hybrid network was presented, focusing on energy transactions between the systems. The authors proposed a method for optimal system operation, in addition to evaluating the strategy considering a centralized control, and then with distributed control units.

D. Communication Infrastructure

Figure 1 shows the MG communication infrastructure. The DER units have a local communication interface, as recommended by IEEE Std. 1547–2018 [5]. The communication protocol used between the DERs and the CC is based on ModBus TCP, according to IEEE 2030.9–2019 [39]. The ModBus protocol paves the way for the interconnection of DERs from different manufacturers in a single-controllable MG. The SunSpec ModBus protocol [40] has emerged from the commercial alliance of more than 120 companies from the distributed energy industry which seeks “plug & play” integration for the sector. The communication between the power node device and the CC occurs via ModBus RTU (RS-485) at a baud rate of 115200 bits/s. Both Modbus protocols run with a polling rate of 5 s.

The Node-RED programming tool was used to develop the CC algorithm (i.e., modified power-based control–MPBC [36]). For the sake of stability, the secondary control must be processed at a lower rate than the traffic of data through the communication network. Then, the MPBC algorithm is executed once every minute because the SMA Sunny Island inverter inherits high latency in updating its output power after having received a power command via the ModBus TCP port.

Finally, communication between the database/supervisory and the CC is carried out once every minute via HTTP protocol, as shown in Figure 1. This ensures the interoperability of the MG with external agents, such as the MGO and/or DSO.

E. Database and Supervisory

The data generated during the MG operation are handled by a supervisory and data acquisition system, in order to evaluate the behavior of the overall MG. The Raspberry PI obtains through the Modbus TCP channel the power, voltage and state of charge, among other information, from the sensors in the MG, and then transfers these data to a private server. Such data are sent via HTTP protocol, and are processed and stored in parallel in this server, as shown in Figure 1. The data are available via authentication of users to visualize the MG behavior using reports and graphics generated in real time.

The database is used to evaluate the MG operation and to manage the middle- and long-term power dispatchability. A free data storage service provided by Google (i.e., Firebase) is used to store the data processed during the MG operation. The data access and the visual platform were devised in JavaScript language using the React library.

3. Centralized MG Control and Operating Modes

This section describes the coordinated control that is used in the single-controllable MG capable of regulating the grid active/reactive power flow, steering phase-to-phase DERs in three-phase four-wire grids and sharing power proportional to the inherent capability of each inverter. The MG performs self-consumption, energy-time shift, island mode and grid-support services without knowledge of grid parameters.

A. Microgrid Control Algorithm

The intrinsic feature of the implemented single-controllable MG (i.e., the connection of three DERs in delta configuration and the measurement of electrical quantities at the CC in star connection) has required modifications in the MG control over the previous version of PBC [37]. Thus, the modified power-based control (MPBC) presented in [36] is applied. Figure 4 schematically summarizes the cyclic operational steps of the MPBC algorithm, which are detailed in Appendix A. The MPBC algorithm, developed in Node-RED, is presented in Appendix B.

B. Full exploitation of different battery banks in the MG

If the single-controllable MG is endowed with different battery banks in terms of age and/or technology, then the power sharing cannot be just proportional to the DERs' power capacity; it must also consider the usable energy. Thus, it is required to maintain usable energy equalization among all battery banks dispersed throughout the MG, in order to reach their maximum and minimum SOC values in about the same instant of time.

Thereby, the scaling coefficients are weighted in terms of usable energy in order to guarantee the maximum exploitation of the battery banks. The CC gathers the usable energy of each bank, and then computes them as in (1), shown as follows:

$$E_{avg}(k) = \frac{E_{DER_{ab}}(k) + E_{DER_{bc}}(k) + E_{DER_{ca}}(k)}{J(k)} \quad (1)$$

Therefore, the α_p is calculated according to (2), and thereupon broadcasted to every j th DER.

$$\text{if } P_{DERt_{mn}}^{min}(k) \leq P_{DERt_{mn}}^*(k+1) \leq P_{DERt_{mn}}^{max}(k) \text{ thus}$$

$$\alpha_{P_{mn}} = \frac{P_{DERt_{mn}}^*(k+1)}{P_{DERt_{mn}}^{max}(k)} \cdot \frac{E_{DERt_{mn}}(k)}{E_{avg}(k)} \quad (2)$$

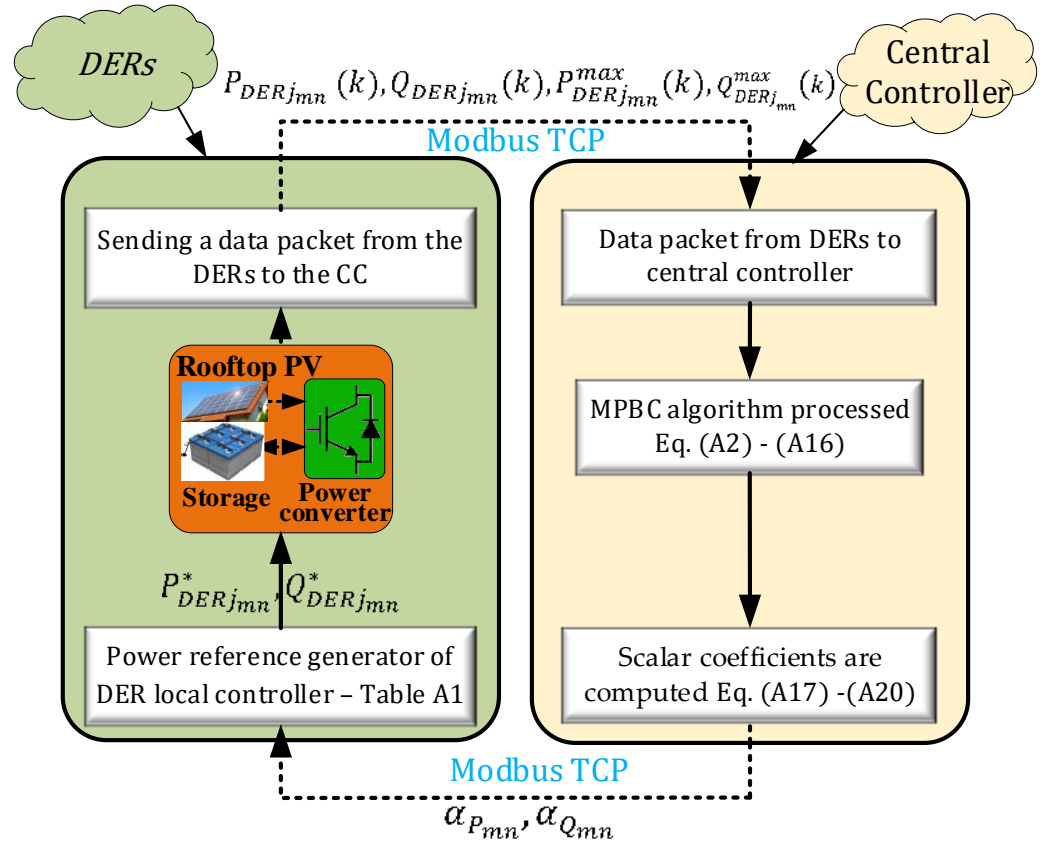


Figure 4. Flowchart of the proposed MPBC execution sequence.

C. Single-Controllable Microgrid Operating Modes

The single-controllable MG uses different operating modes according to its targets, such as economical (*self-consumption, energy time shift*), electrical technical constraints (*peak-shaving*), reliable operation (*island mode*) and upstream power quality enhancement (*grid operational support*). The main operating modes are described as follows:

1. *Self-consumption (SC)*: this mode minimizes the power flow exchanged between the MG and the upstream grid, thereby maximizing the use of renewables. Under normal operation of voltage, frequency and energy resources, the grid power flow is zero and the MG operates in a manner that is virtually disconnected from the mains, minimizing the impact on the upstream power system.
2. *Energy time shift (ETS)*: this involves storing energy into the batteries when costs are low, and delivering energy when the costs are high. It maximizes the profit and shortens the payback period of DERs. In Brazil, the price of energy is about 3–4 times more expensive during 17–20 h (*peak time*) than for outside this range. Then, it is expected to store energy from the PV power plant and then self-supply the local loads between 17–20 h. The *peak-shaving* service is similar to ETS, but takes into account the peak load demand in order to alleviate the upstream feeders.
3. *MG islanded operation (IO)*: this may occur intentionally or non-intentionally; the former is planned for MG stability, whereas the latter is used for continuous power supply during main grid absence. During the MG IO, the grid-forming converter provides voltage reference to the grid-following ones, and the non-critical loads are shed by means of remotely controlled breakers that are spread over the MG feeders.

4. *Grid operational support (GOS)*: it enhances the power quality of the upstream grid based on active/reactive power responses as a function of frequency/voltage deviations. It is basically the freq/watt, volt/var and volt/watt functions applied to the MG PCC with the upstream grid. Moreover, it can also compensate for load imbalances by properly steering the phase-to-phase DERs.

4. Experimental Results

The experimental single-controllable MG based on commercial devices is shown in Figures 1 and 2. The MG uses the hierarchical control of Section 1-B and the MPBC algorithm of Appendix A. It is endowed with a communication infrastructure as described in Section 2-C and the supervisory/data acquisition system of Section 2-D. The MG operation is validated under the SC, ETS, IO and GOS modes. The maximum and minimum SOC values of each battery bank have been defined, based on their inherent technology features such as life cycle versus depth of discharge. Therefore, the SOC limits for the three battery banks are as follows: lithium-ion 25–95%, lead-acid 65–90% and sodium–nickel 30–95%. On the basis of these battery capacities (Section 2), their corresponding released capacity values are 350 Ah, 330 Ah and 260 Ah, respectively. Finally, the power flow in the results follows the notation criteria defined in Figure 1.

A. Self-consumption

The MG self-consumption service steers the grid power flow to zero, even under load and PV power variations, as shown in Figure 5 (load and PCC active power) and Figure 6 (α_{pm} and DER active power). The experiment begins with the control disabled and the MG importing 2 kW per phase in the PCC to supply its loads, and at the instant of 360 s the MPBC is enabled, so the power in the PCC goes to zero. At instant 630 s, the MG load is disconnected and after 45 s the power flow in the PCC returns to zero. At $t = 930$ s, the PV plant begins injecting 1.5 kW per phase of the MG, taking the load power to a negative value as a result of the direction of the power flow. Then, at instant 1235 s, the PV plant is disconnected from the MG. Power control in the PCC inherits the latency of the communication system, in addition to the time required for the SMA inverters to update their parameters via ModBus TCP. In practical implementation, this procedure takes about 45 s. Given this intrinsic latency of SMA inverters, the CC control cycle is set to 60 s in order to ensure stable MG operation, as discussed in [41].

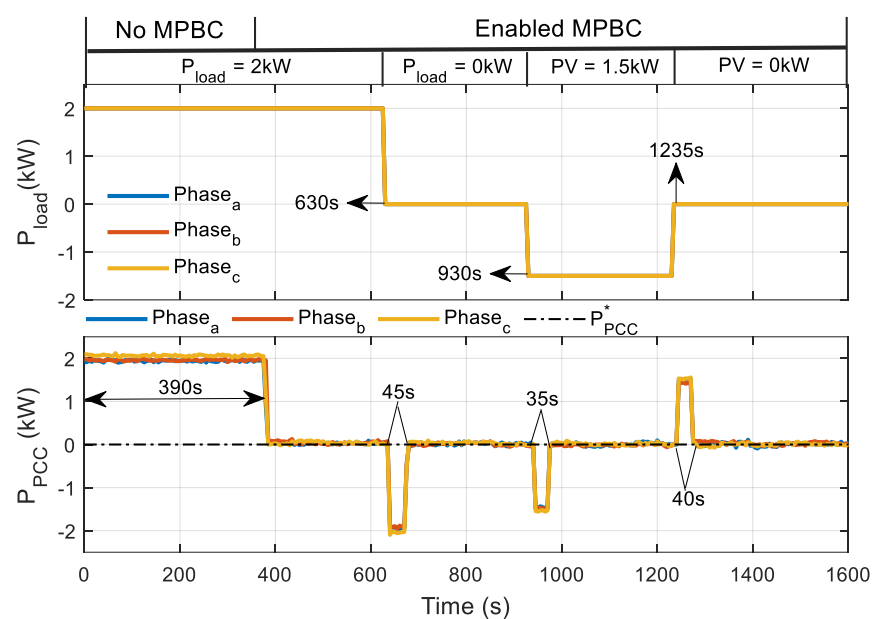


Figure 5. Load power and PCC active power during self-consumption mode.

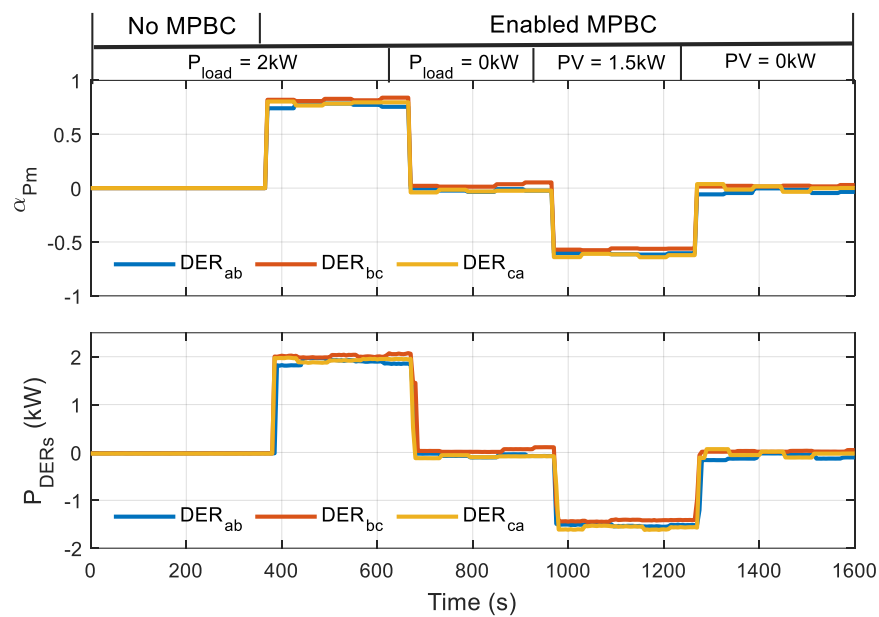


Figure 6. Behavior of coefficients $\alpha_{P_{mn}}$ and DER active power during SC mode.

B. Energy time shift

The challenge of this service is to completely deliver the energy during the 17–20 h period of costly energy prices, considering three different battery technologies: lead-acid, lithium-ion and sodium–nickel. In order to fully maximize the power delivery, the three battery banks must inject power that is proportional to the overall usable energy stored in the system, as well as consider their individual released capacities. Thus, this prevents a battery bank from reaching its minimum limit of SOC before the other battery banks. If this occurs, it will interrupt the ETS service or cause imbalances in power injected into the upstream grid.

Figure 7 shows the output power, charged energy, discharged energy, SOC values of each battery bank and PCC power. The battery charging process begins at around 6 am with a power of 2.5 kW. As a result of the different battery technologies used, the charging process ends at different times. In addition, it is observed that the sodium–nickel battery reached its voltage limit twice during the charging process, and the central controller acted by reducing the power during charging, which contributed to it ending the process last. From the top graphic, one can see that the ETS service begins at 17 h and lasts up to 20 h, delivering about 5 kW per battery bank. At 17 h, the three battery banks show maximum SOC values, as shown in the fourth graphic. During the 3 h of ETS operation, the battery banks delivered power in proportion to their released capacities according to (2). One can see that the three battery banks achieved their minimum SOC values at 20 h. Thus, the three battery banks were fully exploited, independent of their technology and inner features.

Finally, the round-trip efficiency is computed as the ratio between the discharging net energy delivered and the total charging energy consumed. Then, Figure 7 shows the round-trip efficiency for the battery banks: lithium-ion, 93%, lead-acid, 89% and sodium–nickel 88%. During the seven months of operation (from June to December of 2021), the average round-trip efficiency values were 93% (lithium-ion), 85% (lead-acid) and 81% (sodium–nickel). These numbers are in accordance with values found in literature that show 90–95% for lithium-ion, 80–85% for lead acid and 75–90% for sodium-nickel [42].

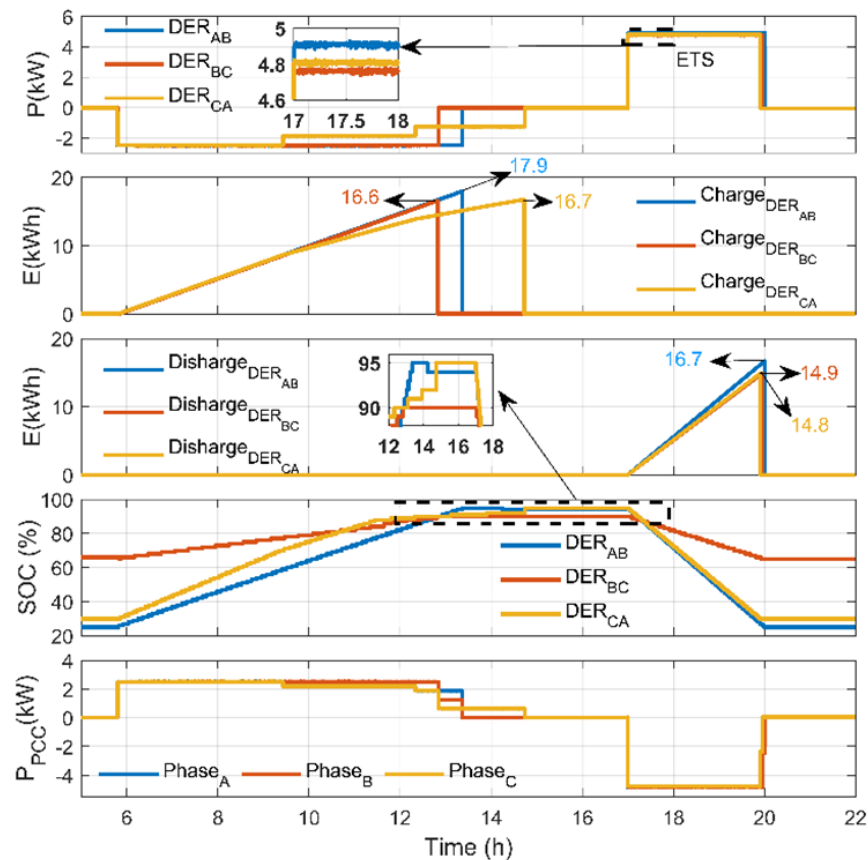


Figure 7. Results of the energy time shifting operation: DER power, charged DER energy, discharged DER energy and SOC value during the energy time shift using three different battery banks: lithium-ion (DER_{ab}), lead-acid (DER_{bc}) and sodium–nickel (DER_{ca}).

C. Grid operational support

The MG GOS enhances the power quality in the upstream feeders, responds to voltage/frequency variations and compensates for load imbalances. The voltage and frequency variations are set by a programmable grid source emulator.

C.1. Reactive power response to voltage variation

In this experiment, the ability of the microgrid to perform GOS to the electrical grid upstream is verified through the reactive control in the PCC in the face of voltage variations. The results of Figure 8 (PCC voltage and PCC reactive power) and Figure 9 (α_{Qm} and DER reactive power) validate the response of the single-controllable MG to voltage variations. The operation begins with the control disabled; at 330 s the MPBC is enabled, and the PCC reactive power reference is precisely regulated according to its reference at 600 VAR. Then, the mains voltage is reduced to 119 V in 650 s, being restored to its nominal value in 945 s, remaining so until 1245 s when it is raised to 140 V, and finally restored to its nominal value in 1560 s. The reactive power reference is set at the DC (i.e., secondary control layer) based on a conventional steady-state volt-var function and the voltage measurement at the MG PCC. The reactive power reference on the PCC is set to -1500 VAR during voltage sag and to 1500 VAR during voltage rise. It is observed that the volt-var function is applied at the connection point of the MG with the upstream grid, and not at the connection point of the DERs with the MG. The latency in reactive power control is due to the delay in the communication system and the time required to update the parameters of the SMA inverter via the Modbus TCP network, with the latter having the greatest impact. The DERs have their power output defined by the scalar coefficient α_{Qm} . The output power is equal to the power in the PCC because no load is connected to the MG during this experiment.

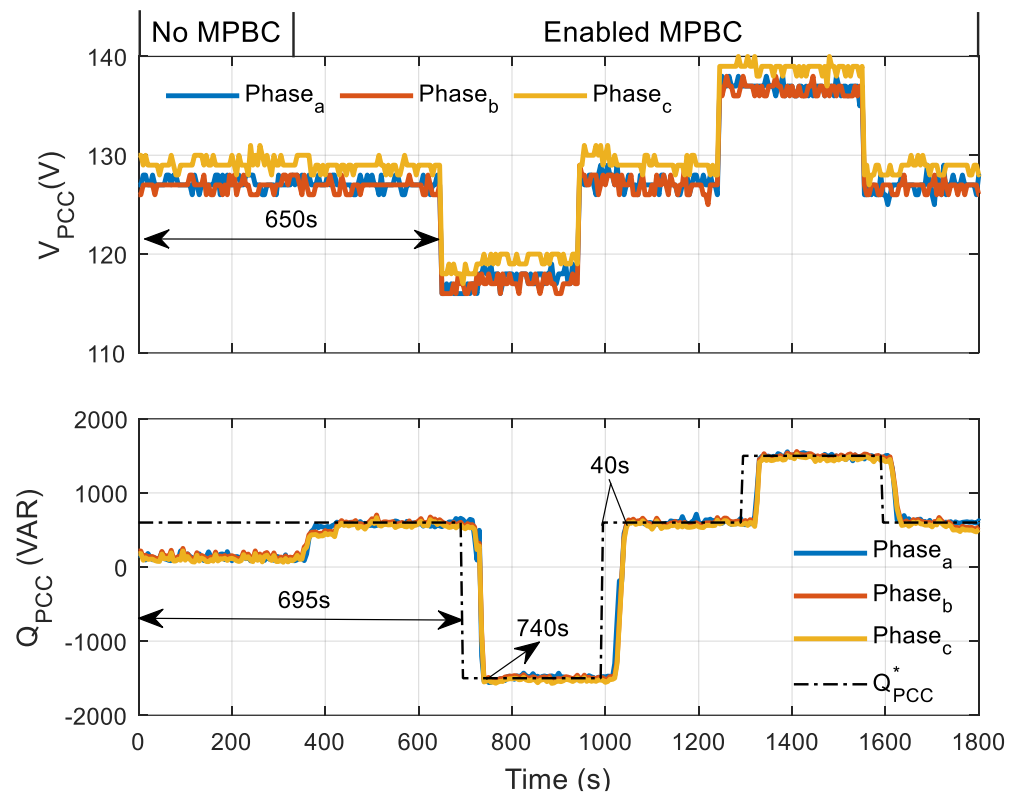


Figure 8. Voltage and PCC reactive power during GOS mode, in terms of voltage variation.

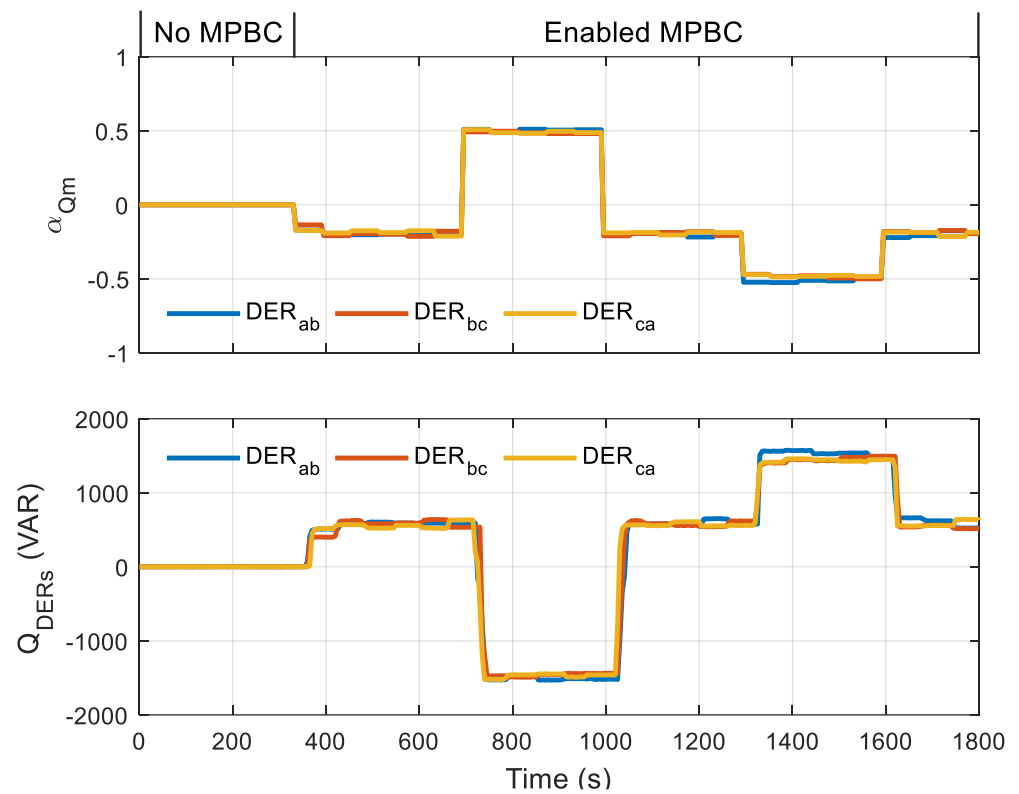


Figure 9. Behavior of coefficients α_{Qm} and DER reactive power during GOS mode, in terms of voltage variation.

C.2. Active power response to frequency variation

The response of the single-controllable MG to frequency variation is validated in Figure 10, where the grid frequency, PCC active power and α_{Pm} coefficient are shown. The frequency drops to 59.6 Hz at 280 s, restores at 600 s, increases to 60.4 Hz at 860 s, and then finally restores to 60 Hz at 1150 s. The reference of active power is set in the CC based on a conventional steady-state frequency-watt function and on the frequency measured at MG PCC by a phase-locked loop (PLL) [43]. The reduction in the voltage frequency in the PCC indicates a high-power demand in the upstream grid, and at that moment the MG begins exporting 2 kW per phase in order to relieve the system, and to contribute to the reestablishment of the frequency. On the other hand, when the frequency increases in the PCC, it means there is an operation with low demand on the utility grid, and at that moment the central control changes the PCC reference so that 2 kW per phase is imported to the MG. Such active power modulation is a response to upstream grid variations, or to frequency deviations in an island of multiple MGs [44].

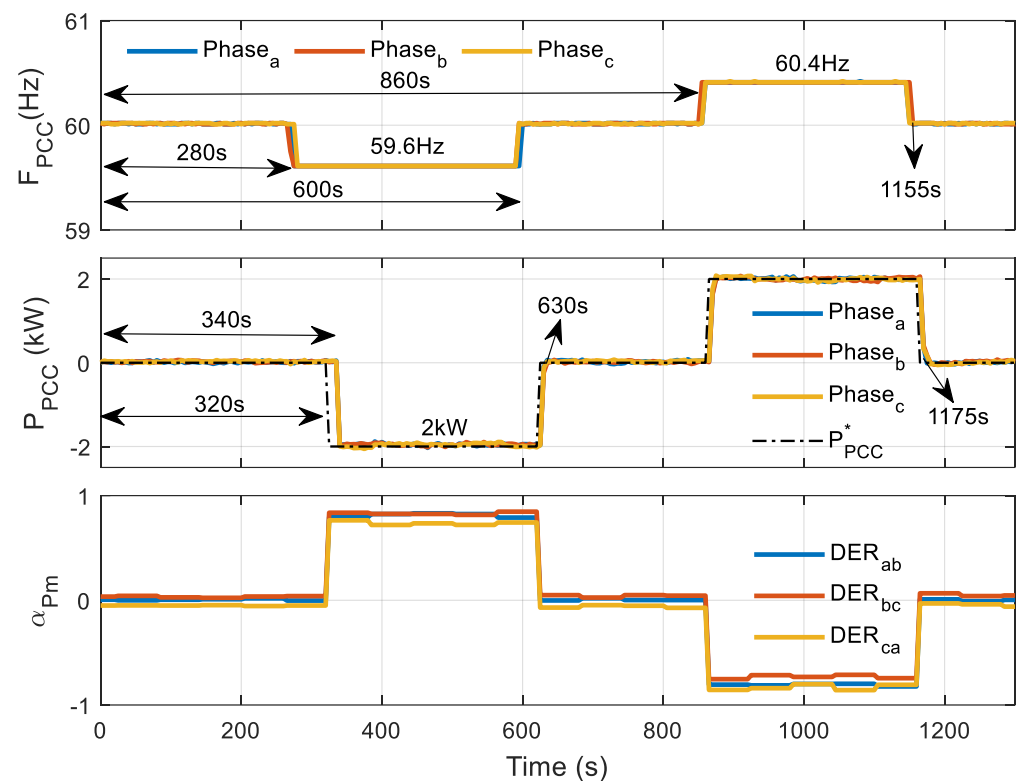


Figure 10. Line frequency, PCC active power and coefficients $\alpha_{P_{mn}}$ during GOS mode, in terms of frequency variation.

C.3. Load unbalance compensation

This case study evaluates the capability of the single-controllable MG to operate balanced at PCC even under load/generation imbalance. Figure 11 shows the PCC power and DERs power when the MG supplies an unbalanced resistive load: 0.5 kW, 1 kW and 1.5 kW in phases a, b and c, respectively. At 200 s, the MPBC is enabled, and the PCC power is controlled at $P_{PCC}^* = 1$ kW. Then, the PCC power reference changes to zero (at 680 s), to 0.5 kW at 860 s and to zero again at 1100 s, delivering always balanced power to the upstream grid. Finally at 1380 s, the MPBC is disabled, resulting in unbalanced power at the PCC. It is interesting to note that to achieve imbalance compensation in the PCC, the DERs must operate unbalanced, as shown in Figure 11.

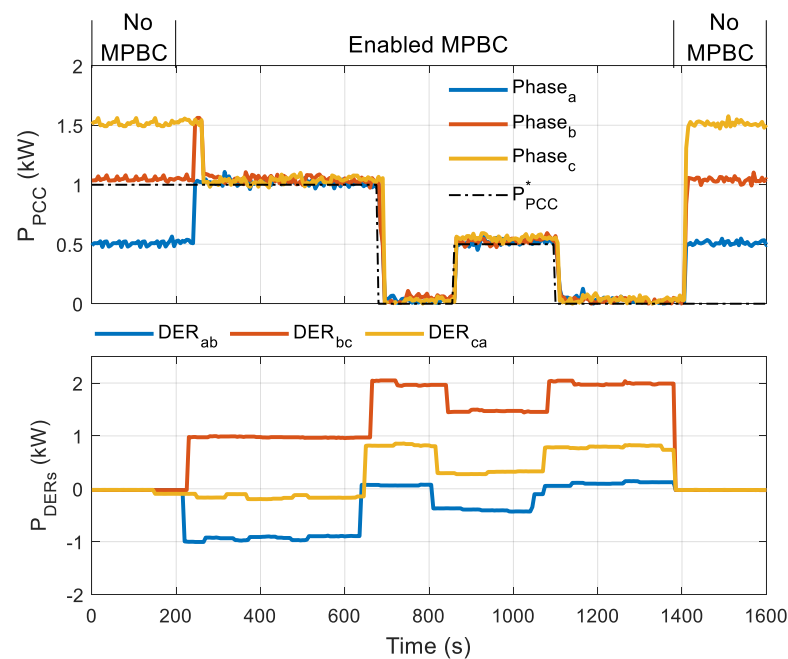


Figure 11. Imbalance compensation: PCC active power and DER power during GOS mode.

D. Islanded operation

The MG islanded operating mode increases the level of electrical reliability to critical loads. The transitioning from grid-connected to island mode may occur with a short-term voltage interruption or smooth (i.e., seamless), depending on the hardware. MGs are subject to different fault conditions, as are other elements of the electrical system. Therefore, this experiment aims to evaluate the operation of the microgrid during a critical fault (i.e., transition from connected to islanded mode). Figure 12 shows the experimental results obtained during a non-intentional islanding of the implemented MG (breaker CB₁ of Figure 1 is suddenly open). This transitioning requires 6 s. The SMA Sunny Island inverter when set to grid-connected mode requires about 5–7 s to restore voltage to critical loads [45]. Then, it does not fulfill the requirements of uninterruptible power supply, as per IEC 62040.

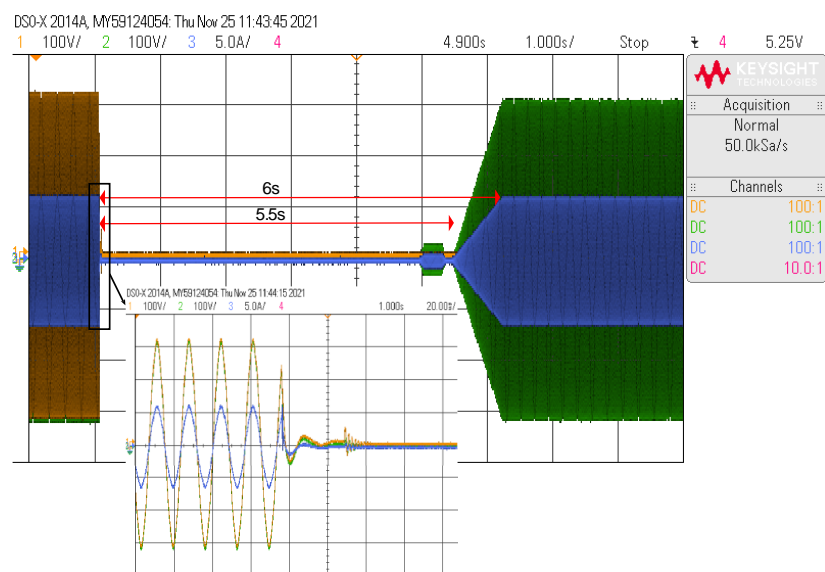


Figure 12. Transitioning from grid-connected to islanded MG mode: grid voltage (yellow), inverter output voltage (green) and load current (blue).

5. Conclusions

This paper presented the practical implementation of a single-controllable MG based on commercial devices and open-source software. This approach creates possibilities for greater developments in MG labs at universities, allowing more interaction between researchers and students with technology. The setup was validated under typical operating conditions, highlighting its capability to provide ancillary services (voltage, frequency and power imbalance mitigation) at the point of the MG connection with the upstream grid.

The coordinate control strategy based on the average usable energy for the three battery technologies is validated. It guaranteed that battery banks reach their minimum SOC values at about the same instant in time. The lithium-ion battery showed the best performance in terms of round-trip efficiency, 93% over 85% (lead-acid) and 81% (sodium–nickel). Lithium-ion battery technology also showed the best compromise between market availability, cost, energy density and usability.

The centralized MG controller based on the MPBC was deployed using the Node-RED programming tool in a Raspberry PI. This combination made possible a relatively fast prototyping of the microgrid central controller and the supervisor, as well as easy interaction with the Modbus communication protocol. However, for applications that require greater processing power as well as reliability and redundancy in the central control, the use of programmable logic controllers (PLCs) appears to be a good option.

In order to update the power variables through the ModBus communication port, the SMA Sunny Island inverter inherits a delay of about one minute. It limits the MG response time on the order of a few minutes, which is quite reasonable for services based on steady-state quantities, rather than on dynamic services as the reactive current support at the voltage level to create virtual inertia. The islanding transfer service cannot rely on communication, and must be managed by the SMA inverters themselves. However, when they are set in grid-connected mode, six seconds are required to restore voltage, which may not be suitable for some types of critical loads. Therefore, it does not fulfill the requirements of uninterruptible power supply, as per IEC 62040.

The integration of new commercial devices from different manufacturers, as well as the use of different communication protocols, are part of the continuity proposals of this research.

Author Contributions: Conceptualization, G.L.R., D.I.B., J.H.O. and L.S.A.; methodology, G.L.R., D.I.B., J.H.O., L.S.A. and B.J.C.F.; software, G.L.R., D.I.B., J.H.O. and L.S.A.; validation, G.L.R., D.I.B., J.H.O. and L.S.A.; formal analysis, G.L.R., D.I.B. and B.J.C.F.; investigation, G.L.R., L.S.A. and D.I.B.; resources, G.L.R., D.I.B., B.J.C.F. and J.H.O.; data curation, G.L.R., D.I.B. and L.S.A.; writing—original draft preparation, G.L.R., D.I.B., J.H.O. and L.S.A.; writing—review and editing, G.L.R., D.I.B. and L.S.A.; visualization, G.L.R., D.I.B., J.H.O., L.S.A. and B.J.C.F.; supervision, D.I.B. and B.J.C.F.; administration, D.I.B. and B.J.C.F.; funding acquisition, G.L.R., D.I.B. and B.J.C.F. All authors have read and agreed to the published version of the manuscript.

Funding: This work has been developed under the Research and Technological Development Program of the Electric Energy Sector regulated by ANEEL under the title “Technical and commercial arrangements for the insertion of energy storage systems in the Brazilian electric sector”, project id ANEEL PD-00553-0046/2016, with Petrobras as the project proponent and funder. The authors also thank the financial support from Universidade federal de Itajubá (UNIFEI) and Fundação de Amparo à Pesquisa do Estado de Minas Gerais (FAPEMIG) under Grant PPM-00587-18 for the payment of the article processing charges.

Institutional Review Board Statement: Not applicable.

Informed Consent Statement: Not applicable.

Data Availability Statement: Not applicable.

Conflicts of Interest: The authors declare no conflict of interest. The funders had no role in the design of the study; in the collection, analyses, or interpretation of data; in the writing of the manuscript; or in the decision to publish the results.

Appendix A

The MPBC description is split into the following: (1) data packet sent from DERs to CC; (2) MPBC algorithm processed in the CC and scaling coefficients (α_{Pmn} and α_{Qmn}) broadcasted to DERs; (3) full exploitation of different battery banks in the MG; and (4) setting the local power references of DERs. The subscripts m and n stand for pairs of phases a, b and c , and J is the number of DERs running in the MG control.

1. Data packet from DERs to central controller

The MPBC operates based on the status of the DERs, which are gathered by the CC at the beginning of each control cycle, k . The status of each DER_{mn} , where $mn = ab, bc, ca$, comprises the actual output power $[P_{DERjmn}(k), Q_{DERjmn}(k)]$; the maximum capacity to provide active power at that instant $[P_{DERjmn}^{max}(k)]$; the maximum capacity to absorb active power from the grid $[P_{DERjmn}^{min}(k)]$ —given by a negative value; maximum idle power capacity available at that instant $[Q_{DERjmn}^{max}]$ given by (1), where $A_{DERjmn}(k)$ is the rated apparent power of DER; and the actual usable energy $[E_{DERjmn}(k)]$.

$$Q_{DERjmn}^{max}(k) = \sqrt{A_{DERjmn}(k)^2 - P_{DERjmn}(k)^2} \quad (A1)$$

2. MPBC algorithm processed into the CC

Once the CC has gathered all the required data packets from every j th DER, the status of the whole MG is computed in terms of power quantities. The first step computes the total power/energy quantities per mn -phase-to-phase, such as the following:

$$\begin{aligned} & [P_{DERt_{mn}}, Q_{DERt_{mn}}, P_{DERt_{mn}}^{max}, Q_{DERt_{mn}}^{max}, E_{DERt_{mn}}] \\ &= \sum_{j=1}^J [P_{DERjmn}, Q_{DERjmn}, P_{DERjmn}^{max}, Q_{DERjmn}^{max}, E_{DERjmn}] \end{aligned} \quad (A2)$$

The second step converts the phase-to-neutral PCC power terms measured and calculated by the CC in star connection (P_{PCC_a} , P_{PCC_b} and P_{PCC_c}) to phase-to-phase PCC power terms ($P_{PCC_{ab}}$, $P_{PCC_{bc}}$ and $P_{PCC_{ca}}$) in delta representation, by means of matrix A in (A3). The reactive power quantities conversion from phase-to-neutral to phase-to-phase is similar, as shown in (A4):

$$\begin{bmatrix} P_{PCC_{ab}} \\ P_{PCC_{bc}} \\ P_{PCC_{ca}} \end{bmatrix} = \underbrace{\begin{bmatrix} 1 & 1 & -1 \\ -1 & 1 & 1 \\ 1 & -1 & 1 \end{bmatrix}}_A \cdot \begin{bmatrix} P_{PCC_a} \\ P_{PCC_b} \\ P_{PCC_c} \end{bmatrix} \quad (A3)$$

$$\begin{bmatrix} Q_{PCC_{ab}} \\ Q_{PCC_{bc}} \\ Q_{PCC_{ca}} \end{bmatrix} = \underbrace{\begin{bmatrix} 1 & 1 & -1 \\ -1 & 1 & 1 \\ 1 & -1 & 1 \end{bmatrix}}_A \cdot \begin{bmatrix} Q_{PCC_a} \\ Q_{PCC_b} \\ Q_{PCC_c} \end{bmatrix} \quad (A4)$$

where P_{PCC_m} and Q_{PCC_m} are the active and reactive power measured per m -phase at the grid side of the PCC, as shown in Figure 1.

The third step estimates the MG power demand based on power balance (i.e., the sum of load and losses is equal to the generated power). Then, the active and reactive power terms drawn between phases in the MG during the control cycle k are estimated $[P_{Lt_{mn}}(k), Q_{Lt_{mn}}(k)]$ as per (A5)–(A10):

$$P_{Lt_{ab}}(k) = P_{PCC_a}(k) + P_{PCC_b}(k) - P_{PCC_c}(k) + P_{DERt_{ab}}(k) \quad (A5)$$

$$P_{Lt_{bc}}(k) = -P_{PCC_a}(k) + P_{PCC_b}(k) + P_{PCC_c}(k) + P_{DERt_{bc}}(k) \quad (A6)$$

$$P_{Lt_{ca}}(k) = P_{PCC_a}(k) - P_{PCC_b}(k) + P_{PCC_c}(k) + P_{DERt_{ca}}(k) \quad (A7)$$

$$Q_{L_{ab}}(k) = Q_{PCC_a}(k) + Q_{PCC_b}(k) - Q_{PCC_c}(k) + Q_{DER_{ab}}(k) \quad (A8)$$

$$Q_{L_{bc}}(k) = -Q_{PCC_a}(k) + Q_{PCC_b}(k) + Q_{PCC_c}(k) + Q_{DER_{bc}}(k) \quad (A9)$$

$$Q_{L_{ca}}(k) = Q_{PCC_a}(k) - Q_{PCC_b}(k) + Q_{PCC_c}(k) + Q_{DER_{ca}}(k) \quad (A10)$$

Fourth step—the CC computes the active and reactive power references [$P_{DER_{mn}}^*(k+1)$, $Q_{DER_{mn}}^*(k+1)$] to be provided to the j th DER in the next control cycle ($k+1$), as per (11)–(16):

$$P_{DER_{ab}}^*(k+1) = P_{L_{ab}}(k) - P_{PCC_a}^*(k+1) - P_{PCC_b}^*(k+1) + P_{PCC_c}^*(k+1) \quad (A11)$$

$$P_{DER_{bc}}^*(k+1) = P_{L_{bc}}(k) + P_{PCC_a}^*(k+1) - P_{PCC_b}^*(k+1) - P_{PCC_c}^*(k+1) \quad (A12)$$

$$P_{DER_{ca}}^*(k+1) = P_{L_{ca}}(k) - P_{PCC_a}^*(k+1) + P_{PCC_b}^*(k+1) - P_{PCC_c}^*(k+1) \quad (A13)$$

$$Q_{DER_{ab}}^*(k+1) = Q_{L_{ab}}(k) - Q_{PCC_a}^*(k+1) - Q_{PCC_b}^*(k+1) + Q_{PCC_c}^*(k+1) \quad (A14)$$

$$Q_{DER_{bc}}^*(k+1) = Q_{L_{bc}}(k) + Q_{PCC_a}^*(k+1) - Q_{PCC_b}^*(k+1) - Q_{PCC_c}^*(k+1) \quad (A15)$$

$$Q_{DER_{ca}}^*(k+1) = Q_{L_{ca}}(k) - Q_{PCC_a}^*(k+1) + Q_{PCC_b}^*(k+1) - Q_{PCC_c}^*(k+1) \quad (A16)$$

where $P_{PCC_m}^*(k+1)$ and $Q_{PCC_m}^*(k+1)$ are, respectively, the active and reactive power references of the phase power flow through the PCC. These power references can be balanced or not, and are set based on the MG tertiary layer, which is beyond the scope of this paper.

Finally, in the fifth step, the CC calculates the scalar coefficients for the j th DER connected between the phases “ mn ” $\alpha_{P_{mn}}$ and $\alpha_{Q_{mn}}$ (all ranging in the interval $[-1, 1]$). The active power is controlled by the coefficient α_P , while the reactive power is controlled by the coefficient α_Q .

The scalar coefficients are computed according to (A17)–(A20), depending on the values of $P_{DER_{mn}}^*$ and $Q_{DER_{mn}}^*$ in comparison to the maximum ($P_{DER_{mn}}^{max}$) and minimum ($P_{DER_{mn}}^{min}$) values. The sign of α_P indicates an operation of delivering (if positive) or storing (if negative) active power, while the sign of α_Q commands generation of capacitive (if negative) or absorption of inductive (if positive) reactive power. After the calculation of α_P and α_Q , they are broadcasted to every j th DER.

$$\text{if } P_{DER_{mn}}^*(k+1) < P_{DER_{mn}}^{min}(k) \text{ thus } \alpha_{P_{mn}} = -1 \quad (A17)$$

$$\text{if } P_{DER_{mn}}^{min}(k) \leq P_{DER_{mn}}^*(k+1) \leq P_{DER_{mn}}^{max}(k) \text{ thus } \alpha_{P_{mn}} = \frac{P_{DER_{mn}}^*(k+1)}{P_{DER_{mn}}^{max}(k)} \quad (A18)$$

$$\text{if } P_{DER_{mn}}^*(k+1) > P_{DER_{mn}}^{max}(k) \text{ thus } \alpha_{P_{mn}} = 1 \quad (A19)$$

$$\alpha_{Q_{mn}} = \frac{Q_{DER_{mn}}^*(k+1)}{Q_{DER_{mn}}^{max}(k)} \quad (A20)$$

3. Power reference generator of DER local controller

After the DERs have received the scalar coefficients sent by the CC, they calculate their individual active and reactive power references that are to be used in their inner control loops (i.e., primary control layer), according to their individual maximum power capacity. Table A1 shows the setting of the local power references for different status of coefficients.

Table A1. Power references of the DERs implemented in each local controller.

| Scalar Coefficients | <i>j</i> th DER Power References |
|-------------------------------|--|
| $\alpha_{Pmn} = -1$ | $P_{DERjmn}^* = P_{DERjmn}^{min}$ |
| $-1 < \alpha_{Pmn} \leq 0$ | $P_{DERjmn}^* = \alpha_{Pmn} \cdot P_{DERjmn}^{min}$ |
| $0 < \alpha_{Pmn} < 1$ | $P_{DERjmn}^* = \alpha_{Pmn} \cdot P_{DERjmn}^{max}$ |
| $\alpha_{Pmn} = 1$ | $P_{DERjmn}^* = P_{DERjmn}^{max}$ |
| $-1 \leq \alpha_{Qmn} \leq 1$ | $Q_{DERjmn}^* = \alpha_{Qmn} \cdot Q_{DERjmn}^{max}$ |

Appendix B

Figures A1 and A2 show the MPBC algorithm developed in the Node-RED tool and implemented in the Raspberry PI 3 B+.

```

1
2 //declaration of variables
3 var PLa=0;
4 var PLb=0;
5 var PLc=0;
6 var QLa=0;
7 var QLb=0;
8 var QLc=0;
9 var a1=0;
10 var a2=0;
11 var a3=0;
12 var b1=0;
13 var b2=0;
14 var b3=0;
15 var PS =0;
16 var data = new Date();
17
18 //Definition of maximum active power values of SMAs
19 var Pmaxa = 2500;
20 var Pmaxb = 2500;
21 var Pmaxc = 2500;
22 flow.set('Pmaxa',Pmaxa);
23 flow.set('Pmaxb',Pmaxb);
24 flow.set('Pmaxc',Pmaxc);
25
26
27 //Calculation of the maximum value of pot. reactive available
28 var Qmaxa = Math.sqrt(6000*6000 - flow.get('Psm77')*flow.get('Psm77'));
29 var Qmaxb = Math.sqrt(6000*6000 - flow.get('Psm73')*flow.get('Psm73'));
30 var Qmaxc = Math.sqrt(6000*6000 - flow.get('Psm72')*flow.get('Psm72'));
31
32 if(Qmaxa>3000)
33 {Qmaxa = 3000;}
34 else
35 {if (Qmaxa<-3000)
36 {Qmaxa = -3000;}
37 }
38 if(Qmaxb>3000)
39 {Qmaxb = 3000;}
40 else
41 {if (Qmaxb<-3000)
42 {Qmaxb = -3000;}
43 }
44
45 if(Qmaxc>3000)
46 {Qmaxc = 3000;}
47 else
48 {if (Qmaxc<-3000)
49 {Qmaxc = -3000;}
50 }
51 flow.set('Qmaxa',Qmaxa);
52 flow.set('Qmaxb',Qmaxb);
53 flow.set('Qmaxc',Qmaxc);
54
55 // Algorithm MPBC
56 if (flow.get('pbc')==1 && flow.get('OSsma77')==235 && flow.get('OSsma73')==
235 && flow.get('OSsma72')==235 && flow.get('start')==1)
57 {
58 PLa = (flow.get('Pga')+flow.get('Pgb')-flow.get('Pgc')+flow.get('Psm77'));
59 a1 = (PLa - flow.get('P0a')) / Pmaxa;
60 if(a1>1)
61 {a1 = 1;}
62 else {
63 if (a1<-1)
64 {a1 = -1;}
65 }
66
67 PLb = (-flow.get('Pga')+flow.get('Pgb')+flow.get('Pgc')+flow.get('Psm73'));
68 a2 = (PLb - flow.get('P0b')) / Pmaxb;
69 if(a2>1)
70 {a2 = 1;}
71 else {
72 if (a2<-1)

```

Figure A1. Part 1 of the MPBC algorithm developed in the Node-RED tool.

```

73         {a2 = -1;}
74     }
75
76     PLc = (flow.get('Pga')-flow.get('Pgb')+flow.get('Pgc')+flow.get('Psm72'));
77     a3 = (PLc - flow.get('P0c')) / Pmaxc;
78     if(a3>1)
79     {a3 = 1;}
80     else {
81         if (a3<-1)
82         {a3 = -1;}
83     }
84
85     QLa = (flow.get('Qga')+flow.get('Qgb')-flow.get('Qgc'))-flow.get('Qsm77');
86     b1 = (QLa - flow.get('Q0a')) / Qmaxa;
87     if(b1>1)
88     {b1 = 1;}
89     else {
90         if (b1<-1)
91         {b1 = -1;}
92     }
93
94     QLb = (-flow.get('Qga')+flow.get('Qgb')+flow.get('Qgc'))-flow.get('Qsm73');
95     b2 = (QLb - flow.get('Q0b')) / Qmaxb;
96     if(b2>1)
97     {b2 = 1;}
98     else {
99         if (b2<-1)
100        {b2 = -1;}
101    }
102
103    QLc = (flow.get('Qga')-flow.get('Qgb')+flow.get('Qgc'))-flow.get('Qsm72');
104    b3 = (QLc - flow.get('Q0c')) / Qmaxc;
105    if(b3>1)
106    {b3 = 1;}
107    else {
108        if (b3<-1)
109        {b3 = -1;}
110    }
111
112    a1 = a2 = a3 = b1 = b2 = b3 = 0;
113    PLa = PLb = PLc = QLa = QLb = QLc = 0;
114    }
115
116    flow.set('a1',a1);
117    flow.set('a2',a2);
118    flow.set('a3',a3);
119    flow.set('b1',b1);
120    flow.set('b2',b2);
121    flow.set('b3',b3);
122
123    var msg1 = {payload : PLa};
124    var msg2 = {payload : PLb};
125    var msg3 = {payload : PLc};
126    var msg4 = {payload : QLa};
127    var msg5 = {payload : QLb};
128    var msg6 = {payload : QLc};
129    var msg7 = {payload : a1};
130    var msg8 = {payload : a2};
131    var msg9 = {payload : a3};
132    var msg10 = {payload : b1};
133    var msg11 = {payload : b2};
134    var msg12 = {payload : b3};
135    var msg13 = {payload : flow.get('pbc')};
136
137    return [msg1, msg2, msg3, msg4, msg5, msg6, msg7, msg8, msg9, msg10, msg11,
138           msg12, msg13];
139

```

Figure A2. Part 2 of the MPBC algorithm developed in the Node-RED tool.

References

1. Lingling Fan and others Microgrid Evolution Solutions. *IEEE Electr. Mag.* **2020**, *8*. [[CrossRef](#)]
2. Bollen, M.H.J.; Hager, M. Power Quality: Interactions Between Distributed Energy Resources, the Grid, and Other Customers. *Electr. Power Qual. Util.* **2005**, *1*, 51–61.
3. Ismael, S.M.; Abdel Aleem, S.H.E.; Abdelaziz, A.Y.; Zobaa, A.F. State-of-the-art of hosting capacity in modern power systems with distributed generation. *Renew. Energy* **2019**, *130*, 1002–1020. [[CrossRef](#)]
4. Fatima, S.; Püvi, V.; Lehtonen, M. Review on the PV hosting capacity in distribution networks. *Energies* **2020**, *13*, 4756. [[CrossRef](#)]
5. *IEEE Std 1547-2018 (Revision IEEE Std 1547-2003)*; IEEE Standard for Interconnection and Interoperability of Distributed Energy Resources with Associated Electric Power Systems Interfaces. IEEE: Piscataway, NJ, USA, 2018; pp. 1–138.

6. Oleinikova, I.; Hillberg, E. Micro vs. MEGA: Trends Influencing the Development of the Power System, Discussion Paper. 2020. Available online: https://www.iea-iscan.org/wp-content/uploads/2020/05/ISGAN_DiscussionPaper_Annex6_microVsMEGA_2020.pdf (accessed on 29 August 2022).
7. Boroyevich, D.; Cvetković, I.; Dong, D.; Burgos, R.; Wang, F.; Lee, F. Future electronic power distribution systems: A contemplative view. In Proceedings of the 2010 12th International Conference on Optimization of Electrical and Electronic Equipment, Basov, Romania, 20–22 May 2010; pp. 1369–1380.
8. Gutiérrez, J.R.L.; Ponce, P.; Molina, A. Real-time power electronics laboratory to strengthen distance learning engineering education on smart grids and microgrids. *Futur. Internet* **2021**, *13*, 237. [[CrossRef](#)]
9. Guo, L.; Abdul, N.M.M.; Vengalil, M.; Wang, K.; Santuzzi, A. Engaging Renewable Energy Education Using a Web-Based Interactive Microgrid Virtual Laboratory. *IEEE Access* **2022**, *10*, 60972–60984. [[CrossRef](#)]
10. Chai, H.; Priestley, M.; Tang, X.; Ravishankar, J. Implementation of microgrid virtual laboratory in a design course in electrical engineering. In Proceedings of the International Conference on Teaching, Assessment, and Learning for Engineering 2020 (IEEE TALE 2020), Takamatsu, Japan, 8–11 December 2020; pp. 509–515. [[CrossRef](#)]
11. Salcedo, R.; Corbett, E.; Smith, C.; Limpaecher, E.; Rekha, R.; Nowocin, J.; Lauss, G.; Fonkwe, E.; Almeida, M.; Gartner, P.; et al. Banshee distribution network benchmark and prototyping platform for hardware-in-the-loop integration of microgrid and device controllers. *J. Eng.* **2019**, *2019*, 5365–5373. [[CrossRef](#)]
12. Wang, J.; Song, Y.; Li, W.; Guo, J.; Monti, A. Development of a universal platform for hardware in-the-loop testing of microgrids. *IEEE Trans. Ind. Inform.* **2014**, *10*, 2154–2165. [[CrossRef](#)]
13. Kotsampopoulos, P.C.; Kleftakis, V.A.; Hatziargyriou, N.D. Laboratory Education of Modern Power Systems Using PHIL Simulation. *IEEE Trans. Power Syst.* **2017**, *32*, 3992–4001. [[CrossRef](#)]
14. Kikusato, H.; Ustun, T.S.; Suzuki, M.; Sugahara, S.; Hashimoto, J.; Otani, K.; Shirakawa, K.; Yabuki, R.; Watanabe, K.; Shimizu, T. Integrated Power Hardware-in-the-Loop and Lab Testing for Microgrid Controller. In Proceedings of the 2019 IEEE Innovative Smart Grid Technologies-Asia (ISGT Asia), Chengdu, China, 21–24 May 2019; pp. 2743–2747. [[CrossRef](#)]
15. Kikusato, H.; Ustun, T.S.; Suzuki, M.; Sugahara, S.; Hashimoto, J.; Otani, K.; Shirakawa, K.; Yabuki, R.; Watanabe, K.; Shimizu, T. Microgrid controller testing using power hardware-in-the-loop. *Energies* **2020**, *13*, 2044. [[CrossRef](#)]
16. Restrepo-Zambrano, J.A.; Ramírez-Scarpetta, J.M.; Orozco-Gutiérrez, M.L.; Tenorio-Melo, J.A. Experimental framework for laboratory scale microgrids. *Rev. Fac. Ing.* **2016**, *2016*, 9–23. [[CrossRef](#)]
17. Laayati, O.; El Hadraoui, H.; Guennoui, N.; Bouzi, M.; Chebak, A. Smart Energy Management System: Design of a Smart Grid Test Bench for Educational Purposes. *Energies* **2022**, *15*, 2702. [[CrossRef](#)]
18. Patra, S.; Madichetty, S.; Basu, M. Development of a smart energy community by coupling neighbouring community microgrids for enhanced power sharing using customised droop control. *Energies* **2021**, *14*, 5383. [[CrossRef](#)]
19. Meng, L.; Savaghebi, M.; Andrade, F.; Vasquez, J.C.; Guerrero, J.M.; Graells, M. Microgrid central controller development and hierarchical control implementation in the intelligent microgrid lab of Aalborg University. In Proceedings of the 2015 IEEE Applied Power Electronics Conference and Exposition (APEC), Charlotte, NC, USA, 15–19 March 2015; pp. 2585–2592. [[CrossRef](#)]
20. Akpolat, A.N.; Yang, Y.; Blaabjerg, F.; Dursun, E.; Kuzucuoglu, A.E. Design Implementation and Operation of an Education Laboratory-Scale Microgrid. *IEEE Access* **2021**, *9*, 57949–57966. [[CrossRef](#)]
21. Nasr-azadani, B.E.; Su, P.; Zheng, W.; Rajda, J.; Cañizares, C.; Kazerani, M.; Veneman, E.; Cress, S.; Wittemund, M.; Manjunath, M.R.; et al. The Canadian Renewable Energy Laboratory: A Testbed for Microgrids. *IEEE Electr. Mag.* **2020**, *8*, 49–60. [[CrossRef](#)]
22. Kermani, M.; Adelmanesh, B.; Shirdare, E.; Sima, C.A.; Carnì, D.L.; Martirano, L. Intelligent energy management based on SCADA system in a real Microgrid for smart building applications. *Renew. Energy* **2021**, *171*, 1115–1127. [[CrossRef](#)]
23. *IEEE 2030.8-2018*; IEEE Standard for the Testing of Microgrid Controllers. IEEE: Piscataway, NJ, USA, 2018. ISBN 9781504446082.
24. Fernandes, N.T.; Rocha, A.; Brandao, D.; Filho, B.C. Comparison of Advanced Charge Strategies for Modular Cascaded Battery Chargers. *Energies* **2021**, *14*, 3661. [[CrossRef](#)]
25. Caldognetto, T.; Tenti, P. Microgrids operation based on master-slave cooperative control. *IEEE J. Emerg. Sel. Top. Power Electron.* **2014**, *2*, 1081–1088. [[CrossRef](#)]
26. Hou, X.; Sun, Y.; Lu, J.; Zhang, X.; Koh, L.H.; Su, M.; Guerrero, J.M. Distributed hierarchical control of AC microgrid operating in grid-connected, islanded and their transition modes. *IEEE Access* **2018**, *6*, 77388–77401. [[CrossRef](#)]
27. Tenti, P.; Caldognetto, T. On microgrid evolution to local area energy network (E-LAN). *IEEE Trans. Smart Grid* **2019**, *10*, 1567–1576. [[CrossRef](#)]
28. Raza, S.A.; Jiang, J. Intra-and Inter-Phase Power Management and Control of a Residential Microgrid at the Distribution Level. *IEEE Trans. Smart Grid* **2019**, *10*, 6839–6848. [[CrossRef](#)]
29. Wu, X.X.; Xu, Y.; Wu, X.X.; He, J.; Guerrero, J.M.; Liu, C.-C.C.; Schneider, K.P.; Ton, D.T. A Two-Layer Distributed Cooperative Control Method for Islanded Networked Microgrid Systems. *IEEE Trans. Smart Grid* **2020**, *11*, 942–957. [[CrossRef](#)]
30. Abedini, H.; Caldognetto, T.; Mattavelli, P.; Tenti, P. Real-time validation of power flow control method for enhanced operation of microgrids. *Energies* **2020**, *13*, 5959. [[CrossRef](#)]
31. Nelson, J.R.; Johnson, N.G. Model predictive control of microgrids for real-time ancillary service market participation. *Appl. Energy* **2020**, *269*, 114963. [[CrossRef](#)]
32. Callegari, J.M.S.; Pereira, H.A.; Brandao, D.I. *Coordinated Volt-Var Control in Microgrids*; IEEE: Piscataway, NJ, USA, 2021.

33. Guerrero, J.M.; Vasquez, J.C.; Matas, J.; De Vicuña, L.G.; Castilla, M. Hierarchical control of droop-controlled AC and DC microgrids-A general approach toward standardization. *IEEE Trans. Ind. Electron.* **2011**, *58*, 158–172. [[CrossRef](#)]
34. Carpintero-Rentería, M.; Santos-Martín, D.; Guerrero, J.M. Microgrids literature review through a layers structure. *Energies* **2019**, *12*, 4381. [[CrossRef](#)]
35. Elmouatamid, A.; Ouladsine, R.; Bakhouya, M.; Kamoun, N.E.; Khaidar, M.; Zine-Dine, K. Review of control and energy management approaches in micro-grid systems. *Energies* **2020**, *14*, 168. [[CrossRef](#)]
36. Reis, G.; Liberado, E.; Maraf, F.; Sousa, C.; Silva, W.; Brandao, D. Model-Free Power Control for Low-Voltage AC Dispatchable Microgrids with Multiple Points of Connection. *Energies* **2021**, *14*, 6390. [[CrossRef](#)]
37. Brandao, D.I.; Caldognetto, T.; Marafão, F.P.; Simões, M.G.; Pomilio, J.A.; Tenti, P. Centralized Control of Distributed Single-Phase Inverters Arbitrarily Connected to Three-Phase Four-Wire Microgrids. *IEEE Trans. Smart Grid* **2017**, *8*, 437–446. [[CrossRef](#)]
38. Mohamed, M.A.; Abdullah, H.M.; Al-Sumaiti, A.S.; El-Meligy, M.A.; Sharaf, M.; Soliman, A.T. Towards Energy Management Negotiation between Distributed AC/DC Networks. *IEEE Access* **2020**, *8*, 215438–215456. [[CrossRef](#)]
39. *IEEE 2030.9-2019*; IEEE Recommended Practice for the Planning and Design of the Microgrid. IEEE: Piscataway, NJ, USA, 2019.
40. Specification, S.P. *SunSpec Modbus IEEE 1547-2018 Profile Specification and Implementation Guide SunSpec Profile Specification*; SunSpec Alliance: San Jose, CA, USA, 2018; pp. 1–35.
41. Caldognetto, T.; Brandao, D.I.; Buso, S.; Tenti, P. Power-Based Control of Low-Voltage Microgrids. *IEEE J. Emerg. Sel. Top. Power Electron.* **2015**, *3*, 1056–1066. [[CrossRef](#)]
42. Eller, A.; Giovinetto, A. *Comparing the Costs of Long Duration Energy Storage Technologies*; National Grid Ventures: London, UK, 2019.
43. Pádua, M.S.; Deckmann, S.M.; Marafão, F.P. Frequency-adjustable positive sequence detector for power conditioning applications. *PESC Rec.-IEEE Annu. Power Electron. Spec. Conf.* **2005**, *2005*, 1928–1934. [[CrossRef](#)]
44. Al-Tameemi, Z.H.A.; Lie, T.T.; Foo, G.; Blaabjerg, F. Control strategies of DC microgrids cluster: A comprehensive review. *Energies* **2021**, *14*, 7569. [[CrossRef](#)]
45. SMA Planning Guidelines “SMA FLEXIBLE STORAGE SYSTEM with Battery-Backup Function: Circuitry Overviews, Schematic Diagrams and Material Lists”. 2019, pp. 1–54. Available online: <https://files.sma.de/downloads/SI44M-80H-13-BBF-IA-en-10.pdf> (accessed on 29 August 2022).